aerospace

MDPI

Article

Hygrothermal Aging and Strength Prediction of CFRP Single-Lap Joints: Experiments and Physics-Constrained Neural Networks

Xuan-Qi Ren [1], Jia-Mu He [2], Yu-Ya Wang [3], Liang Chang [1,4], Xiao-Hua Nie [1], Li-Long Luo [1], Guo-Fan Zhang [1] and Wei Feng [1,4,*]

[1] National Key Laboratory of Strength and Structure Integrity, Aircraft Strength Research Institute of China, Xi'an 710065, China; renxuanqi@163.com (X.-Q.R.)
[2] Xi'an ASN Technology Group Co., Ltd., Xi'an 710072, China; 18392595793@163.com
[3] 93208th Unit of the Chinese People's Liberation Army, Beijing 100076, China
[4] School of Aeronautics, Northwestern Polytechnical University, Xi'an 710072, China
* Correspondence: fengwei@nwpu.edu.cn; Tel.:+86-15029048078

Abstract

Adhesively bonded carbon-fiber-reinforced polymer (CFRP) joints offer efficient load transfer and weight-saving potential in aerospace structures. The simple geometry of single-lap joints (SLJs) makes them useful for examining bond durability, although the effects of hygrothermal aging on their performance have not been sufficiently investigated. This research systematically integrates moisture absorption experiments, mechanical testing, finite element modeling (FEM), and deep neural network (DNN) modeling to provide a comprehensive analysis of moisture absorption behavior, strength degradation, and the evolution of failure modes within the adhesive layer. Initially, three types of adhesives were aged under various hygrothermal aging conditions to investigate their moisture absorption behavior and mechanical performance after aging. The tensile strength and modulus of the adhesives decreased linearly with increasing moisture uptake. In addition, hygrothermal aging tests were conducted on SLJs. Results demonstrated a significant reduction in joint shear strength during aging, accompanied by a transition in failure mode from cohesive to interfacial. Subsequently, a hygrothermally coupled FE model was developed using the experimental data and combined with a cohesive zone model to simulate joint strength evolution. The FE model achieved a calculation error within 5%. To address the high computational cost associated with finite element analysis of hygrothermal aging in SLJ structures and to enhance the physical interpretability of data-driven models, a novel prediction strategy was introduced. A three-stage serial neural network model was constructed using experimental and simulation data, with the quadratic stress criterion and power-law criterion embedded as physical constraints. Compared to unconstrained models, this physics-constrained neural network exhibited superior prediction accuracy and stability. The proposed method offers a valuable reference for the design and evaluation of the durability of CFRP bonded structures.

Keywords: single-lap joints; hygrothermal aging; cohesive zone model; physics-constrained neural networks; failure morphology

Check for updates

Academic Editor: Qingguo Fei

Received: 26 August 2026
Revised: 30 September 2026
Accepted: 8 October 2026
Published: 15 October 2026

Copyright: © 2026 by the authors. Licensee MDPI, Basel, Switzerland. This article is an open access article distributed under the terms and conditions of the Creative Commons Attribution (CC BY) license.

1. Introduction

Adhesively bonded composite structures are increasingly applied in aircraft design and repair. This is due to their advantages, including high bonding efficiency, continu-

ous stress distribution, excellent fatigue resistance, and significant weight reduction [1,2]. During aircraft service, bonded structures can encounter humid ground storage, rain or condensation, and temperature changes between ground and flight conditions. Moisture transport and temperature-dependent material properties can therefore affect joint durability. The single-lap joint (SLJ) is the most widely used bonded structure, owing to its simple geometry and effective load-transfer capability. However, these structures suffer from aging effects during long-term service exposure to temperature fluctuations, moisture, and salt spray [3,4]. Based on the degradation mechanisms of composite materials, aging-induced failures can be classified into four types: CFRP fiber fracture, cohesive failure within the adhesive layer, interfacial debonding, and mixed-mode failure. As moisture absorption increases, the adhesive's mechanical properties deteriorate, which is a primary influencing factor [5]. Furthermore, adhesives exhibit significant differences in hygrothermal susceptibility, degradation mechanisms, and failure modes [6]. Nevertheless, conventional tensile failure tests on SLJ structures do not include additional characterization of the adhesive. Therefore, the structural failure mechanisms caused by variations in hygrothermal environmental parameters remain inadequately understood.

Finite element modeling (FEM) provides detailed physics-based simulations. However, incorporating hygrothermal effects remains a major challenge in FEM [7]. Moisture diffusion in composites under hygrothermal environments is primarily affected by the degree of resin matrix cure, temperature, humidity, and specimen stress [8]. Integrating hygrothermal aging-induced material degradation as a damage factor to establish a UMAT material model is an effective approach for investigating the impact of aging on the mechanical properties of composites [9–13]. Nevertheless, this requires a clear prior understanding of moisture diffusion behavior and the degradation patterns in material mechanical properties [14–16]. Fick's law and its modified forms can describe moisture diffusion. Researchers have employed Fickian diffusion models and test data to develop simulation models for analyzing the residual performance of aged structures [17–20]. Validated under specific conditions, these models effectively evaluate the effects of hygrothermal environments on joint performance. To determine the residual strength of joints, progressive damage finite element models have been developed that use damage factors to characterize material degradation. Calibrated with static test data from aged adhesives, these models can accurately predict the static response of aged joints [21]. However, extremely high computational costs limit the application of FEM in long-term hygrothermal aging analysis, making it difficult to cover the entire design space. Therefore, there is an urgent need for a highly efficient and accurate method to analyze the strength of structures subjected to long-term hygrothermal aging. Parametric FE studies can become computationally demanding when many combinations of geometry, material properties, and exposure history are considered, motivating the use of surrogate prediction approaches.

Machine learning accurately processes large datasets. Yet it requires massive data and suffers from poor physical interpretability. Integrating the two methods—FEM and machine learning (ML)—combines their respective merits. High-fidelity data are generated using finite element analysis and then used by machine learning to forecast material properties and failure behavior throughout an extended design space. This mixed framework enables large-scale dataset analysis and accurate prediction outputs [22]. It has markedly advanced research on composite failure prediction [23] and composite fracture toughness [24], fully demonstrating its great potential in composite material investigations. Although progress has been made in bonded joint analysis, most existing studies merely characterize failure attributes under standard conditions [25]. Quantitative analytical results relating to practical engineering applications remain insufficient.

In summary, existing models are mostly based on failure data collected under ambient temperature and humidity conditions. They rarely consider the temporal coupling characteristics of aging time and moisture absorption. Furthermore, they fail to embed damage evolution equations into the network. Currently, there is no predictive framework that can both utilize high-fidelity FEM data and embed the physical criteria for adhesive layer damage as hard constraints within the neural network architecture. To address these issues, this study establishes an integrated strategy combining experiments, simulations, and machine learning. Based on experimental and high-fidelity physics-based simulation data, a three-stage serial neural network framework with physics-based loss constraints is proposed. This framework enables highly efficient and accurate prediction of the strength of hygrothermally aged SLJ structures, as well as the analysis of their variation trends.

2. Materials and Methods

2.1. Specimen Preparation

2.1.1. Adhesive Sample Preparation

The sample dimensions were determined in accordance with ISO 527-2:2012 [26]. The mold was designed as illustrated in Figure 1a; the adhesive was placed inside and cured within a polytetrafluoroethylene mold under vacuum conditions at room temperature for 24 h. The prepared samples are depicted in Figure 1b. Three types of adhesives were studied, namely Araldite 2015, Lord-320/322, and Loctite EA9460.

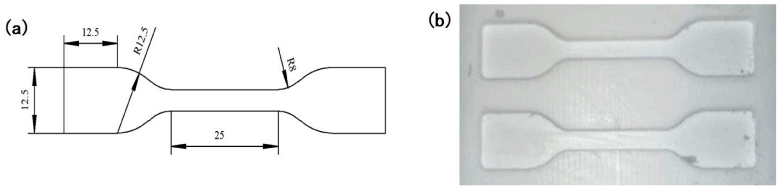


Figure 1. Design and fabrication of adhesive dogbone components: (**a**) design of dogbone components; (**b**) the completed adhesive test specimen after forming.

2.1.2. Preparation of Bonding Structure Specimens

Adhesive dogbone tests provided the constitutive parameters for the adhesive material, while SLJ structural tests were designed to capture the moisture absorption behavior under structural constraint. All subsequent bonded structures were single-lap joints. Their geometric dimensions are shown in Figure 2a. The composite plates consisted of T800 carbon fiber. The ply sequence was $[0]_{16}$. The composites were obtained from Shaanxi Tianqi New Composite Material Technology Co., Ltd., Xi'an, China. The Araldite 2015 adhesive was used. The basic mechanical properties of the composite are listed in Table 1. The mechanical properties of the composite materials are summarized in Table 2 according to the manufacturer's datasheet and have been reported in a previous work [27]. Before bonding, the adherends were cleaned with alcohol and sandpaper. The joints were then cured in a mold. A 0.1 mm spacer was used to control the adhesive thickness. Curing was conducted in a vacuum at room temperature for 24 h. The preparation process is illustrated in Figure 2b. The final test specimens are shown in Figure 2c.

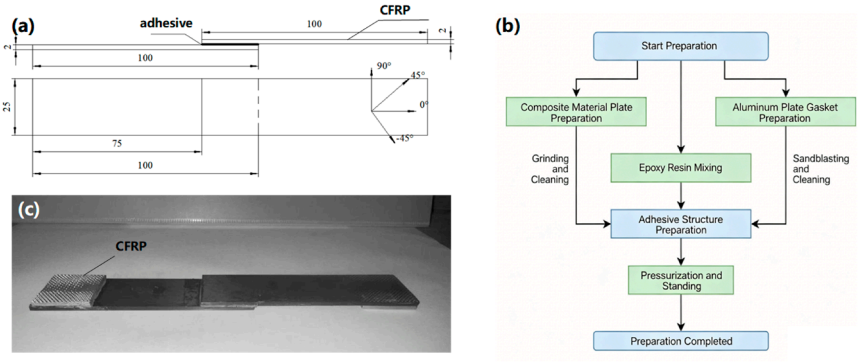


Figure 2. Design and manufacturing process of SLJ test specimens: (**a**) test sample design; (**b**) forming process flow diagram; (**c**) manufactured test piece.

Table 1. Hygrothermal test conditions.

NUM	Temperature (°C)	Relative Humidity (%)
1	23	100% RH
2	65	100% RH
3	45	100% RH

2.2. Hygrothermal Aging Test Procedures

Accelerated hygrothermal aging tests were conducted. The objective was to investigate the moisture absorption characteristics and residual performance of the bonded structures. Different adhesives and composites were evaluated. A 101-00BS constant temperature test chamber was used (Figure 3), which was fabricated by Shaoxing Supo Instrument Co., Ltd., Shaoxing, Zhejiang, China. The specific test conditions are summarized in Table 2. A FA1004 precision electronic balance (Shanghai Shunyu Hengping Scientific Instrument Co., Ltd., Shanghai, China) was used to measure the moisture uptake of the specimens. The planned test duration was 20 days. Moisture uptake was measured every 5 days. The measurement interval was shortened appropriately during the initial stage.

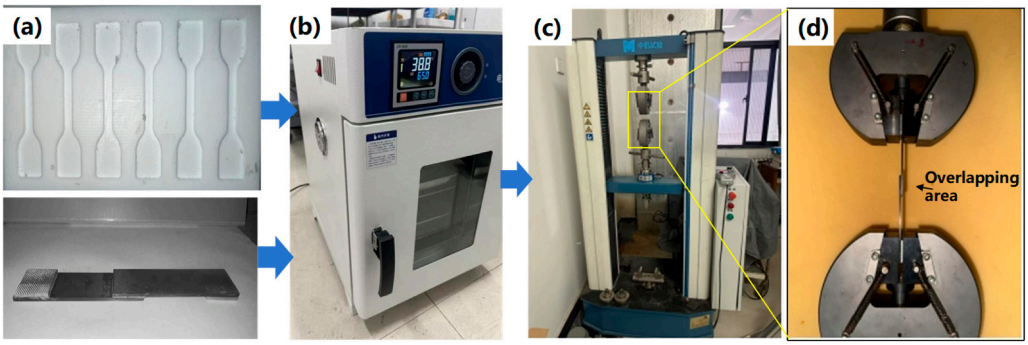


Figure 3. Schematic of the tensile testing process considering moisture absorption: (**a**) prepared specimens; (**b**) hygrothermal conditioning; (**c**) tensile testing machine; (**d**) loading configuration of the specimens.

Table 2. The basic mechanical properties of the composite [27].

MAT	E_1 (MPa)	$E_2 = E_3$ (MPa)	$G_{12} = G_{13}$ (MPa)	G_{23} (MPa)	X_T (MPa)	X_C (MPa)	Y_T (MPa)	Y_C (MPa)	S_{12} (MPa)
T800	146,360	7370	3300	1329	2387	1375	68	135	107

During the hygrothermal test, the main objectives were to measure the changes in moisture absorption and the resulting strength decline of the adhesive, calculate the moisture absorption diffusion rate and saturated moisture absorption limit, and use the standards and formulas outlined in ASTM D570 to determine the moisture absorption of the samples. The formula used to calculate the moisture absorption rate of the sample after hygrothermal aging (M_t) is as follows:

$$M_t = \frac{W_t - W_0}{W_0} \times 100\% \quad (1)$$

where W_t is the weight of the sample after absorbing moisture, and W_0 is the weight of the sample before hygrothermal aging.

The Fickian model is commonly used to describe the free diffusion of single-phase moisture. This study employs Fick's second law to analyze the moisture diffusion process [28]. The governing equation is expressed as follows:

$$\frac{\partial C}{\partial t} = \frac{\partial}{\partial x}\left(D_x \frac{\partial C}{\partial x}\right) + \frac{\partial}{\partial y}\left(D_y \frac{\partial C}{\partial y}\right) + \frac{\partial}{\partial z}\left(D_z \frac{\partial C}{\partial z}\right) \quad (2)$$

The adhesive is an isotropic material. It also has a small thickness. Therefore, the diffusion process can be treated as one-dimensional. Fick's law is simplified as follows:

$$\frac{\partial C}{\partial t} = D\frac{\partial^2 C}{\partial x^2} \quad (3)$$

where C represents the moisture concentration, defined as mass per unit volume; D denotes the moisture diffusion coefficient; and x is the spatial coordinate in the thickness direction. The moisture concentration C(t) can be expressed as

$$\frac{C(t) - C_0}{C_\infty - C_0} = 1 - \frac{4}{\pi}\sum_{n=0}^{\infty} \frac{(-1)^n}{(2n+1)} \exp\left[-\frac{(2n+1)^2 \pi^2 D t}{h^2}\right] \quad (4)$$

In this equation, C_0 is the initial moisture concentration, and C_∞ represents the saturated moisture concentration at the specimen surface. The measured moisture uptake is used to transform this equation. The modified format is given by

$$\frac{M_t}{M_\infty} = \left[1 - \frac{8}{\pi^2}\sum_{j=0}^{\infty} \frac{\exp\left[-(2j+1)^2 \pi^2 \left(\frac{Dt}{h^2}\right)\right]}{(2j+1)^2}\right] \quad (5)$$

where Mt is the moisture uptake at time t. h denotes the material thickness. t is the immersion time. D is the diffusion coefficient. M_∞ represents the equilibrium moisture uptake. In practical applications, the Fickian equation is often simplified. The simplified formula is expressed as

$$\frac{M_t}{M_\infty} = 1 - \exp\left[-7.3\left(\frac{Dt}{h^2}\right)^{0.75}\right] \quad (6)$$

2.3. Mechanical Testing Methods

Tensile tests were conducted after specific hygrothermal conditioning. Adhesive specimens were exposed to a hygrothermal chamber (Figure 3a,b). Tensile strength was evaluated at 5-day intervals. At least three specimens were tested for each interval to ensure repeatability. The results were compared with the initial strength at room temperature. A similar procedure was applied to composite bonded structures. Shear strength was

measured following the same testing protocol. However, the testing interval was adjusted to 10 days. Strength tests were performed in accordance with the ASTM D570-98 standard. A DNS10 electronic universal testing machine (Changchun Research Institute for Testing Machines Co., Ltd., Changchun, China) was utilized (Figure 3c). The loading configuration is illustrated in Figure 3d. The loading rate was strictly controlled at 0.1 mm/min. During the experiments, the specimens were analyzed. The acquired experimental data were also statistically processed.

2.4. FEM Strategies

2.4.1. Moisture Absorption and Diffusion Model

Modeling spatiotemporal variations in the moisture field within the adhesive layer is required before mechanical simulation. A formal similarity exists between Fick's second law and Fourier's heat conduction theorem. Therefore, a temperature field simulation is used to represent variations in the moisture field. This approach enables coupled hygrothermal analysis. First, experimental fitting provides the basis for parameter acquisition. The moisture absorption limit and diffusion rate functions form the basis of the adhesive diffusion process. Second, the specific heat capacity is set to unity. The corresponding moisture diffusion rate is input as thermal conductivity into the heat conduction module. Finally, boundary conditions are established. The environmental temperature gradient is set to the moisture diffusion limit at the corresponding temperature. This procedure ultimately establishes the moisture diffusion model [13].

$$q = -k\nabla T \tag{7}$$

$$J = -D\nabla C \tag{8}$$

where q is heat flux, k is thermal conductivity, T is the thermal field, J is moisture flux, D is moisture diffusivity, C is moisture concentration, and ∇ denotes the spatial gradient.

2.4.2. Performance Degradation of Adhesive

Table 3 presents the Araldite 2015 parameters used for the SLJ model; it does not pool the three adhesives. Tensile strength was obtained from the adhesive tensile tests, and elastic modulus was calculated from the measured stress–strain response. Equations (15)–(17) describe empirical moisture-dependent fitting rather than a failure criterion for identifying material properties. Shear and fracture parameters were adopted from literature-based modeling inputs, with intermediate aging states represented by the linear degradation assumption discussed in Ref. [29].

Table 3. Nominal dry and moisture-saturated parameters for the Araldite 2015 joint model.

Material Parameter	Symbol	Unaged (Dry)	Moisture Saturated
Elastic Modulus (MPa)	E	2340.9	1193.64
Shear Modulus (MPa)	$G_1 = G_2$	560	113.51
Tensile Strength (MPa)	σ_n	17.42	10.63
Shear Strength (MPa)	$\tau_s = \tau_t$	16.9	4.22
Normal Fracture Toughness (N/mm)	G_I	0.41	0.17
Tangential Fracture Toughness (N/mm)	G_{II}	4.20	1.79

2.4.3. Damage Model of the Adhesive Layer

A finite element model was developed to analyze damage resulting from hygrothermal aging. A predefined stress field was introduced to represent the moisture load. The adhesive parameters were assigned based on the moisture uptake. This model synchronously reflects the hygrothermal diffusion process and enables a quantitative evaluation of structural strength evolution. Experimental observations show that all damage occurs in the adhesive layer. The composite structure remains undamaged. Therefore, the damage model focuses on the hygrothermal aging behavior of the adhesive layer. Two common methods exist for modeling adhesive failure. These are the virtual crack closure technique (VCCT) and the cohesive zone model (CZM). The CZM is based on continuum mechanics and damage mechanics. It effectively describes the failure modes and the evolution of damage. Therefore, CZM is introduced into the interface. The simulation uses the stiffness degradation of the cohesive elements. The damage process is divided into two stages: damage initiation and damage evolution.

Material stiffness degrades during the damage initiation stage. Four common criteria are used for this stage. They are the quadratic strain, maximum strain, quadratic stress, and maximum stress criteria. The quadratic stress criterion is widely used for composite bonded joints [30,31]. The criterion is expressed as

$$\left\{\frac{\langle t_n \rangle}{t_n^0}\right\}^2 + \left\{\frac{t_s}{t_s^0}\right\}^2 + \left\{\frac{t_t}{t_t^0}\right\}^2 = 1 \tag{9}$$

where n denotes the normal direction (Mode I fracture), and t and s represent the two tangential directions (Mode II and III fractures). The brackets < > indicate that t_n and ε_n are active only under tensile loading. Under compressive loading, these values are set to zero.

Material properties further degrade during the damage evolution stage. Several CZMs are widely used to describe this process. These include the bilinear, exponential, trapezoidal, and linear-parabolic models. The bilinear model balances computational efficiency and accuracy [30,31] and is sufficient for calculating the bonded structure model. A stiffness degradation parameter D_S is introduced to describe this process. When $D_S = 0$, the material is undamaged. When $D_S = 1$, the material is fully damaged. The parameter is calculated as

$$D_S = \frac{\delta_m^f(\delta_m^{max} - \delta_m^o)}{\delta_m^{max}\left(\delta_m^f - \delta_m^o\right)} \tag{10}$$

where δ_m^{max} is the maximum opening displacement at the calculated node during the loading history, δ_m^f is the opening displacement when D = 1, and δ_m^o is the opening displacement at the onset of damage.

The calculation of δ_m^f is complex. It reflects the fracture energy release rate under complex stress states. The detailed derivation is omitted here. Reference [31] discusses the normal and tangential stiffness. It combines the energy release rate with the failure criteria. It considers whether the normal and tangential stiffness are identical. The power criterion is used for this description:

$$\left(\frac{G_n}{G_n^C}\right)^a + \left(\frac{G_s}{G_s^C}\right)^a + \left(\frac{G_t}{G_t^C}\right)^a = 1 \tag{11}$$

In Equation (11), G_n, G_s, and G_t are the opening and two shear-mode energy components, and G_n^C, G_s^C, and G_t^C are their critical fracture energies, all in N/mm. The exponent α controls the mixed-mode interaction.

2.4.4. Model Construction

Solid elements were used for geometric modeling. The composite plate was modeled as a straight plate with dimensions of 100 mm × 25 mm. The grip shims and the adhesive layer were modeled as square plates with dimensions of 25 mm × 25 mm. Their thicknesses were consistent with those of the single-lap joint specimens. The composite laminate employed eight-node quadrilateral continuum shell elements (SC8R). The grip shims were modeled using eight-node linear hexahedral elements (C3D8R). The adhesive layer utilized eight-node three-dimensional cohesive elements (COH3D8). The mesh configuration is illustrated in Figure 4. A fully fixed constraint was applied to the left side. This completely restrained displacements in all directions. A displacement constraint of 1.5 mm was applied to the right connection surface. The moisture diffusion model and the mechanical model maintained identical geometries and mesh configurations. This ensured consistency between the moisture diffusion process and the structural analysis.

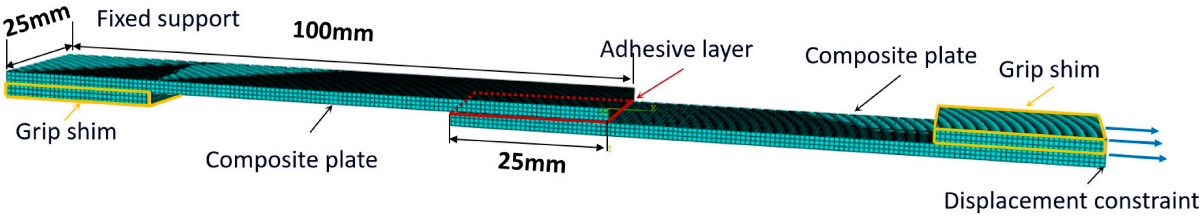


Figure 4. Schematic of the joint simulation model.

The mesh size in the adhesive layer directly affects the accuracy of the calculation results. Camanho conducted a finite element simulation of the DCB test. The study concluded that three elements within the cohesive zone can yield highly repeatable and accurate numerical results. Therefore, the cohesive zone length in the adhesive layer is estimated based on Reference [30].

$$l_{CZ} = ME\frac{G_c}{(\tau^0)^2} \tag{12}$$

The parameter M is determined according to the formula proposed by Reference [32]:

$$M = \frac{9\pi}{32}E\frac{G_c}{(\tau^0)^2} \tag{13}$$

The calculated cohesive zone length ranges from 0.46 mm to 1.15 mm. Thus, the optimal mesh size for the adhesive layer is estimated to be between 0.15 mm and 0.4 mm.

Figure 5 shows that the global reaction-force–displacement curves become close as the mesh is refined to 0.4 mm and below. The load is the total axial reaction force over the loaded grip surface. The displacement is the axial movement of that same surface. The 0.4 mm mesh was retained as a practical choice for the reported global load response. Additional local damage and energy-convergence checks are required before treating this size as universally adequate for the sampled parameter space.

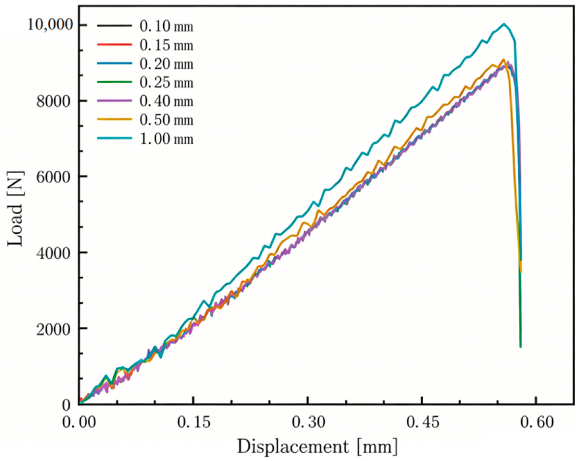


Figure 5. Mesh convergence of the adhesive layer.

2.4.5. Data Generation for Machine Learning

The machine learning dataset was constructed by combining experimental and simulated data. It comprises 200 samples, with experimental data accounting for approximately 10%. The 180 simulated data points were obtained from the simulation model established in the previous section. This model involves 11 key parameters related to geometry, material properties, and environmental factors. Their parameter ranges are listed in Table 4. Within the specified sampling space, 180 samples were generated using Latin hypercube sampling (LHS). A Python 3.11.7 script was then used to automatically generate and invoke a finite element method (FEM) solver. These FE models featured varying geometric configurations and material definitions while maintaining a consistent meshing strategy. The resulting FEM simulation outputs served as the predictive dataset for training the neural network model. It should be noted that 90% of the dataset comes from the same FE model family, so agreement with most training and evaluation samples primarily measures the approximation of that simulator and inherits its constitutive assumptions and validation limits. Predictions outside the parameter ranges defined in Table 4 constitute extrapolations that must be interpreted with caution. Expanding the experimental database, particularly near the sampling-space boundaries, is identified as future work.

Table 4. Sampling range of parameters involved in dataset construction.

Data Type	Influencing Factors	Unit	Range
Material Properties	Elastic Modulus	MPa	1651.85–4980
	Shear Modulus	MPa	560–1660
	Tensile Strength	MPa	20.74–40.45
	Shear Strength	MPa	17.9–31.2
	Mode I Fracture Toughness	N/mm	0.18–0.609
	Mode II Fracture Toughness	N/mm	0.34–4.70
Geometric Dimensions	Adhesive Layer Thickness	mm	0.15–0.25
	Lap Length	mm	20–30
Environmental Factors	Humidity	%	50–100
	Temperature	°C	23–70
	Time	h	0–10,000

2.5. Neural Network Architecture and Data Generation

2.5.1. Serial Neural Network Architecture and Training

The 11 base descriptors are elastic moduls E, shear modulus G, tensile cohesive trength σ_n, shear cohesive strength τ, critical Mode I and Mode II fracture energies G_{Ic} and G_{IIc},

adhesive thickness h_a, overlap length L, relative humidity RH, exposure temperature T, and aging time t. The overlap width is fixed for the present joints and is not a sampled variable in Table 4. Critical fracture energies are material inputs, whereas predicted energy-release-rate components are intermediate responses.

We propose a three-stage prediction model. Connecting multiple neural networks in series decomposes composite strength prediction into related subtasks, allowing each network to learn a specific mapping while passing meaningful intermediate outputs to the next. Rahman [33] cascaded two ANNs to estimate aging conditions before strength prediction, while Wang et al. [34] linked crack-pattern and mechanical-property prediction networks. These studies support using intermediate information to inform subsequent predictions. Following this principle, our serial networks predict interfacial tractions, energy release rates, and joint peak load, enabling physical constraints to be applied at the corresponding stages.

The proposed strategy connects three neural networks in series. Physical constraints are added to the loss function. This method builds a high-quality prediction model. It also greatly reduces the difficulty of parameter optimization. The model structure is shown in Figure 6. The first network maps the base descriptors to three cohesive traction components. The second receives these tractions together with the original descriptors and predicts three mode-dependent energy components. The third uses the predicted energy components and retained original descriptors to predict the joint peak load. Figure 6 summarizes this sequence. Each subnetwork containing one hidden layer with 100 neurons yielded the best balance between expressiveness and stability [34,35]. This physically motivated decomposition is consistent with the broader principle of embedding mechanistic information in learning [25], but those references do not validate this exact three-stage architecture. The Adam optimizer was used with an initial learning rate of 1×10^{-3}, decayed by a factor of 0.5 every 200 epochs; the batch size was 16; training ran for a maximum of 3000 epochs with early stopping (patience of 100 epochs) monitored on the validation MSE to prevent overfitting. All networks were implemented in PyTorch 2.3.1 with a fixed random seed to ensure reproducibility.

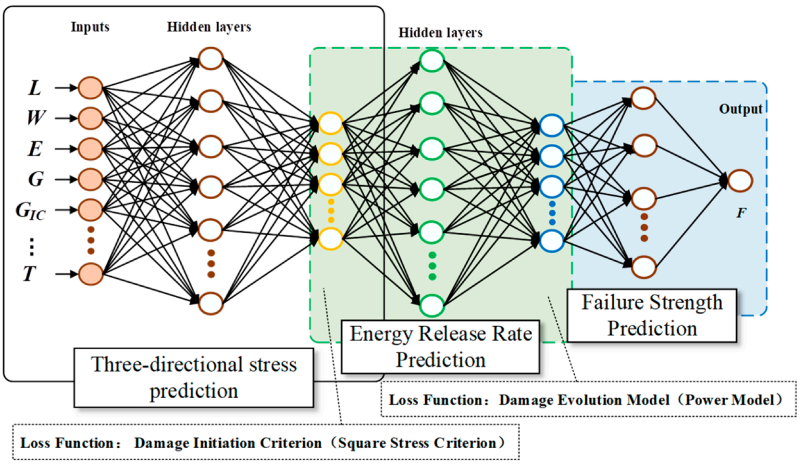


Figure 6. Three-stage serial neural network model with physical boundary constraints.

In the first stage, the predicted normal and shear stresses are substituted into the quadratic stress criterion in Equation (9). For samples representing damage initiation, the difference between the calculated criterion value and its critical value of unity defines the physical residual. The squared residuals are accumulated over the corresponding samples to construct the quadratic-stress constraint loss. The parameters of the first subnetwork are optimized until the prescribed convergence tolerance is satisfied. Its predicted stresses,

together with the relevant original input variables, are then supplied to the second subnetwork. In the second stage, the predicted energy release rates are substituted into the power-law criterion in Equation (11). For samples representing the critical mixed-mode fracture condition, the deviation of the calculated criterion value from unity defines the second physical residual. The accumulated squared residuals constitute the power-law constraint loss. After this stage satisfies its convergence criterion, the predicted energy release rates and the relevant input variables are passed to the third subnetwork to predict joint strength. The revised description also distinguishes the physical residual losses from the prediction error of the final strength output. The two criteria guide the intermediate predictions toward consistency with damage initiation and mixed-mode fracture, respectively, whereas the final prediction loss measures agreement with the reference joint-strength data.

2.5.2. Data Normalization

Before training the machine learning model, data normalization is required. The parameters exhibit inconsistent units and wide value ranges. These variations can cause gradient updates to fall into local loops during iterative training. Therefore, this study normalizes the data to the [0, 1] range using Equation (15).

$$X' = \frac{X - X_{\min}}{X_{\max} - X_{\min}} \tag{14}$$

X is the original input data, x_{min} and x_{max} are the minimum and maximum values of the corresponding features, respectively, X' is the standardized data after normalization, and the final range is [0, 1].

2.5.3. Data Division

The dataset partitioning is illustrated in Figure 7. Three independently randomized 70/30 partitions of the same 200-sample dataset were used, each containing 140 training and 60 held-out samples. This procedure was repeated with random holdout rather than standard three-fold cross-validation. Training and held-out samples are disjoint within a given partition, while samples can recur in different partitions. The original analysis trained three candidate models and retained the candidate with the smallest reported evaluation error. Using held-out performance to select a candidate makes those data part of model selection and can produce optimistic accuracy estimates. The metrics retained in Section 4 are therefore selected model results from the original analysis rather than means over independent folds or an untouched final-test estimate.



Figure 7. Data validation strategy.

3. Hygrothermal Aging Effects and Failure Mechanisms

3.1. Moisture Absorption Characteristics

3.1.1. Experimental Results of the Moisture Absorption Process

Figure 8 illustrates the moisture absorption characteristics of Araldite 2015. Temperature exerts a significant effect on this process. During the initial stage, the moisture diffusion

rate is high. Consequently, the mass change is substantial. Over time, the diffusion rate gradually decreases. The mass increase eventually approaches a plateau. An elevated temperature accelerates the diffusion rate and also increases the overall moisture uptake. For instance, the moisture uptake on day 20 increased from 2.647% at room temperature to 4.378% at 65 °C. As shown in Figure 8a, the equilibrium moisture uptake and moisture diffusion rate of Araldite 2015 increase with temperature. The curves and fitted points are retained from the original measurements; specimen-level uncertainty is not quantified in this figure. When the aging temperature was raised from 23 °C to 65 °C, the moisture diffusion rate increased by approximately 10 times. The equilibrium moisture uptake also increased by 70%. Figure 8b illustrates the linear fitting results. The relationship between the parameters and temperature was evaluated. The R^2 values for both parameters exceed 0.92. This indicates a nearly linear relationship. The moisture absorption parameters vary linearly with the aging temperature. Based on these findings, a linear assumption was adopted to account for the temperature-dependent variations in moisture absorption parameters in the FE model.

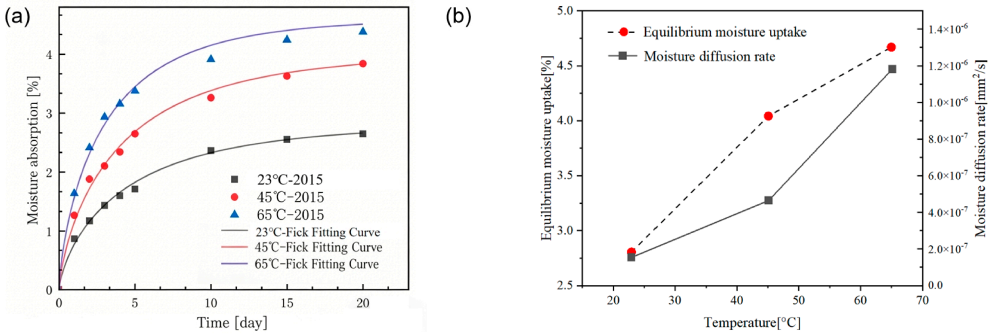


Figure 8. Moisture absorption behavior: (**a**) variation in moisture uptake with time; (**b**) variation in moisture absorption parameters with temperature.

3.1.2. Simulation Results of the Moisture Absorption Process

Figure 9a compares the simulation results with the experimental data for the adhesive specimens. The simulation curve corresponds well to the experimental data. This verifies the feasibility of the moisture absorption model. Subsequently, the established simulation method was applied to the complete bonded joint. A moisture absorption model for the single-lap joint was developed. The side adhesive layer was exposed to moisture. The thermal conductivity parameters of the composite were also set. The moisture absorption limit was normalized. Figure 9b shows that the moisture absorption curve of the overall structure agrees well with the experimental data. The moisture contour of the adhesive layer indicates slow diffusion from the boundary to the interior until the boundary reaches moisture saturation. This is consistent with the moisture diffusion observed in practical engineering. The simulation results show that the moisture absorption of the bonded joint reaches saturation in approximately 250 days.

3.2. Mechanical Properties

3.2.1. Effect of Hygrothermal Aging on the Mechanical Properties of the Adhesive Layer

Tensile failure tests were conducted on the adhesive specimens. The tests were performed at room temperature. Figure 10a,b present the stress–strain curves. The curves include the unaged specimens and those aged for 10 and 20 days. The results indicate a rapid decrease in tensile strength after moisture absorption. The strength gradually approaches a stable value as the moisture uptake reaches saturation.

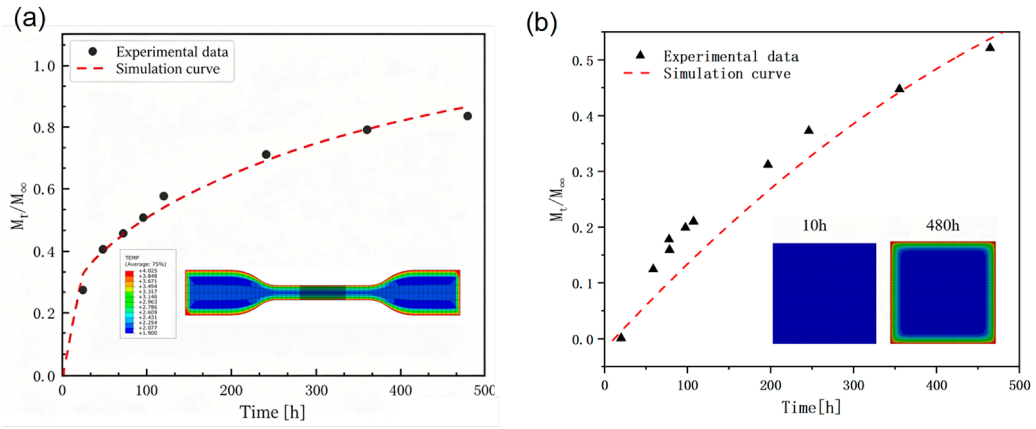


Figure 9. Moisture absorption characteristics: (**a**) moisture absorption curve of the adhesive specimens; (**b**) the moisture absorption curve of the overall structure.

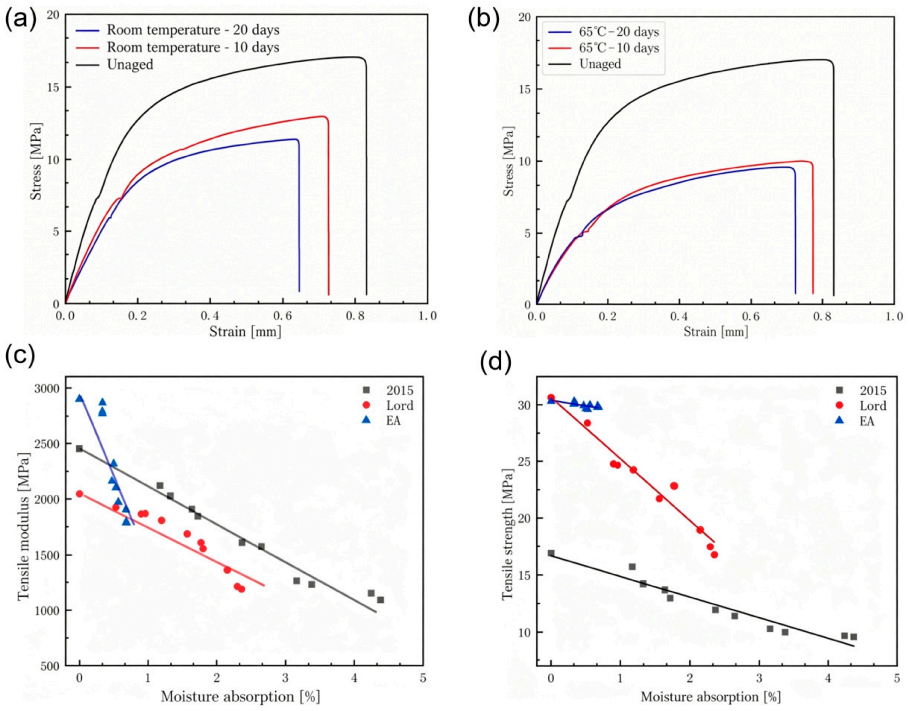


Figure 10. Moisture absorption behavior: (**a**) tensile strength curve of Araldite 2015 at room temperature; (**b**) tensile strength curve of Araldite 2015 at 65 °C; (**c**) tensile strength versus moisture uptake for three adhesives; (**d**) tensile modulus versus moisture uptake for three adhesives.

Figure 10a,b compare three common adhesives: Araldite 2015, EA9460, and Lord-320/322. The tensile strength of all three adhesives decreases as moisture uptake increases. The decreasing trend follows a linear relationship. This linear relationship is assumed to follow the function below:

$$Y = Y_0(1 - K \times M_t) \tag{15}$$

where Y_0 represents the initial tensile modulus and strength. Y denotes the corresponding values at a specific moisture uptake. K is a function related to the material properties. M_t represents the moisture uptake.

Data fitting was performed. The variations in tensile strength and modulus of Araldite 2015 with moisture uptake follow the equation below:

$$\sigma = \sigma_0(1 - (134.09 + 7.153E_0 - 0.0359\sigma_0) \times M_t) \tag{16}$$

$$E = E_0\left(1 - \left(-34.04 + 1.42E_0 - 0.0083{E_0}^2 + 0.0093\sigma_0 - 1.6.\mathrm{e}^{-6}{\sigma_0}^2\right) \times M_t\right) \quad (17)$$

3.2.2. Effect of Hygrothermal Aging on the Mechanical Properties of SLJ Structures

Based on the degradation functions established for the bulk adhesive, the strength evolution of the SLJ structure was subsequently examined. Measurements were conducted on composite bonded joints. Single-lap joint (SLJ) specimens were placed in a controlled hygrothermal environment. Three sets of specimens were removed at regular intervals, and their moisture uptake variations were measured. At days 10 and 20, three specimens were selected for strength testing. The moisture absorption curves are plotted in Figure 11a. The results show that the moisture absorption rate of the SLJ structure is lower than that of the pure adhesive film, although the variation also follows the Fickian diffusion law.

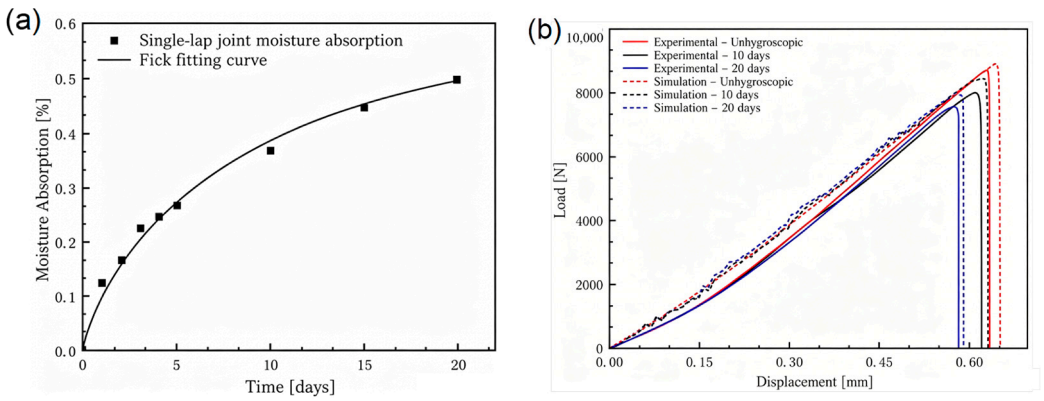


Figure 11. Comparison of the simulation and experimental strength results for the SLJ structure under different hygrothermal coupling times: (**a**) moisture absorption curves of single-lap joints; (**b**) comparison of load-displacement curves after hygrothermal aging.

Tensile tests were performed on the SLJ structures. The shear strength of the specimens was obtained at 45 °C and 100% relative humidity. The variation curve of the shear strength is presented in Figure 11b. The structural strength exhibits a nonlinear variation during hygrothermal aging. After 10 days of aging, the strength decreased by 8.27%. After 20 days of aging, the strength reduction reached 13.41%. Further investigation into the failure modes of the fracture surfaces is required. This is necessary to analyze the mechanism of strength degradation. Table 5 presents the variation in the maximum tensile strength of the SLJ structure and the discrepancies between the simulation and experimental results. The comparison of empirical results shows that the calculation error is within 5%, verifying the model's accuracy. Using the validated modeling method, a parametric model was constructed. This model enables the analysis of bonded joint strength across a wide range of material properties, environmental loads, and geometric dimensions. Furthermore, it provides data support for subsequent machine learning tasks.

Table 5. Comparison of strength variation data for the SLJ structure.

Material Parameters	Experimental Data	Simulation Data	Error
Without hygrothermal aging	8720.67	8979.8	2.89%
10 days of hygrothermal aging	8081.83	8447.98	4.33%
20 days of hygrothermal aging	7565.7	7943.68	4.76%

3.3. Failure Modes and Mechanisms Analysis

3.3.1. Failure Modes

Figure 12a presents the structures without hygrothermal effects. Almost all failures occurred at the adhesive layer connection. This represents a cohesive failure of the adhesive. Minor interface damage was also present. However, its proportion was small. The failure morphology of the hygrothermally aged structures was observed. The failure modes remained concentrated in cohesive and interfacial failures. No damage appeared in the composite plate structure. Figure 12b,c show the evolution of failure modes with prolonged aging time. The interfacial failure proportion increased slightly after 10 days of aging compared with that of the unaged specimens. However, cohesive failure remained the dominant mode. A fundamental shift occurred after 20 days of aging. The failure mode became dominated by interfacial failure with secondary cohesive failure. The proportion of interfacial failure rose sharply with aging time. It increased from an initial 19.74% to a final 87.27%. This transition from cohesive to interfacial failure is essentially the result of combined factors. These factors are moisture diffusion and differential degradation rates.

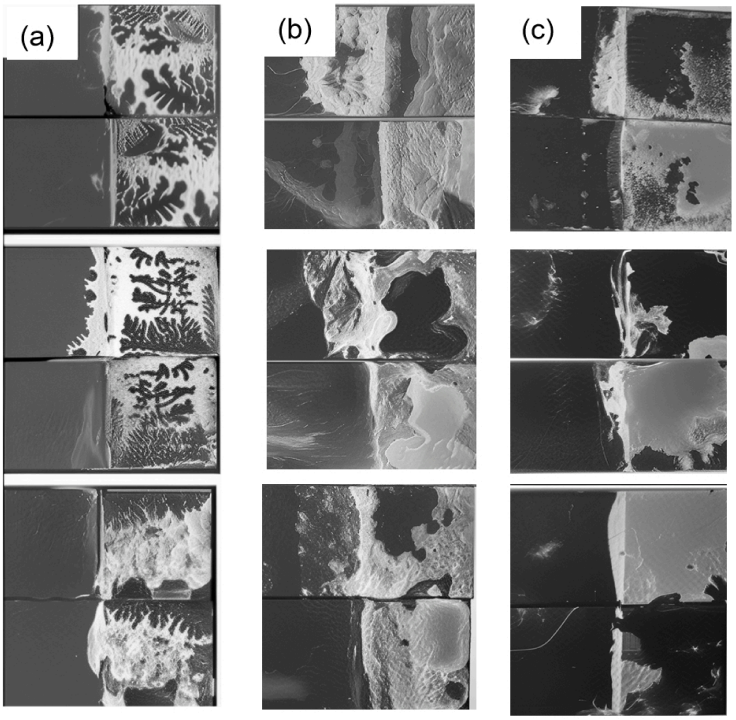


Figure 12. Interfacial failure after different hygrothermal effects: (**a**) the structures without hygrothermal effects; (**b**) 10 days of aging; (**c**) 20 days of aging.

3.3.2. Damage Evolution

To complement the fractographic observations, the stiffness degradation scalar (SDEG) from the FEM simulation was analyzed to reveal the internal damage evolution. Figure 13 shows the SDEG distribution during the failure process of the unaged structure under different loads. The variation in SDEG indicates that degradation of the adhesive layer initiates at locations with the highest moisture absorption on both sides. As the load increases, the stiffness degradation propagates from the edges toward the central region. This propagation direction is consistent with the water diffusion observed in the experimental section.

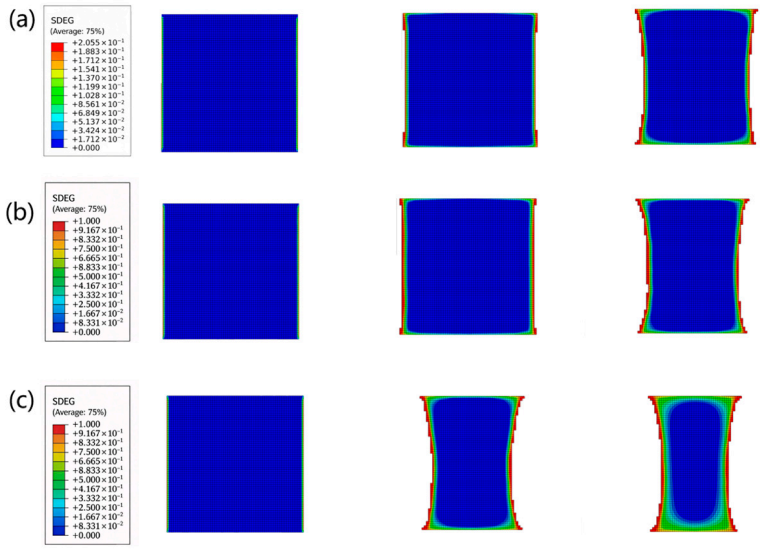


Figure 13. The SDEG distribution during the failure process of the unaged structure under different loads: (**a**) the unaged structure; (**b**) 10 days of hygrothermal aging under a tensile load of 7376.6 N; (**c**) 20 days of hygrothermal aging under the maximum load at structural failure.

3.4. Discussion of Hygrothermal Aging Mechanisms

The experimental results presented in Section 3.1 reveal that both the equilibrium moisture uptake and the diffusion coefficient of the epoxy adhesive increase approximately linearly with temperature. Elevated temperatures enhance molecular chain mobility and create additional micro-voids to accommodate water molecules. Fractographic observations in Section 3.3 show that the proportion of interfacial failure increases sharply after hygrothermal aging. As aging time increases, the failure mode shifts from cohesive to interfacial. This indicates that the degradation rate of the interface is faster than that of the bulk adhesive. This differential degradation can be attributed to the mismatch in hygroscopic swelling between the CFRP adherend and the adhesive, which generates localized tensile stresses at the interface.

A hygrothermally coupled finite element model was established in this study. Its calculation errors were maintained within 5% of the experimental data. The primary advantage of this model lies in its ability to capture the spatiotemporal evolution of moisture concentration within the adhesive layer and the consequent degradation of local stiffness. Nevertheless, the model exhibits certain limitations. The linear degradation assumption was applied to parameters other than modulus and strength. This simplification is particularly problematic for fracture toughness parameters, which typically exhibit nonlinear decay patterns as saturation approaches. This simplification is likely the main cause of the slight deviations observed between the simulation and experimental results during the initial aging stages. These validations are limited to these conditions, and the model's accuracy at other temperature–humidity–time combinations within the sampling space is inferred rather than directly verified, pending broader experimental validation.

4. Data-Driven Prediction and Physics-Constrained Enhancement

4.1. Model Optimization

The selection of the activation function significantly influences the neural network model. Figure 14 compares the training results for three activation functions: sigmoid, tanh, and linear. The two diagonal lines in the figure represent a 10% error band. The results show that the sigmoid function achieves the best overall performance, with a mean

squared error (MSE) of 0.0024 and a coefficient of determination (R^2) of 0.9654. Therefore, the sigmoid function was selected as the activation function for the model.

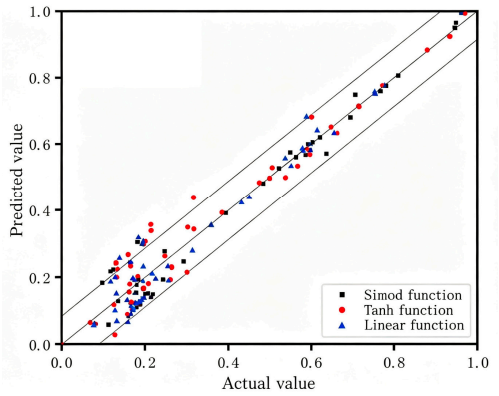


Figure 14. Comparison of model performance using different activation functions.

4.2. Physical Boundary

To investigate the effects of different physical constraints on the prediction results, the squared stress, maximum stress, BK, and power-law criteria were applied as constraints, respectively. Table 6 and Figure 15a compare the performance metrics of the five structural strength prediction models. These metrics include MSE (mean squared error), MAE (mean absolute error), MAPE (mean absolute percentage error), R^2 (coefficient of determination), and IA (index of agreement). These indicators serve as core criteria for evaluating model performance. Specifically, lower values of MSE, MAE, and MAPE indicate lower prediction errors. Conversely, higher values of R^2 and IA are preferred. An R^2 value approaching 1 indicates a high goodness of fit. An IA value approaching 1 signifies high consistency between the predicted and actual values.

Table 6. Comparison of the performance metrics of five structural strength prediction models.

	Maximum and BK Criterion	Maximum and Power Criterion	Quadratic and BK Criterion	Quadratic and Power Criterion	Original Model
MSE	0.0062	0.0064	0.0011	8.857×10^{-4}	0.0024
MAE	0.0609	0.0623	0.0206	0.0198	0.0345
MAPE	26.1988	26.3016	9.8956	7.5538	20.7922
R2	0.8652	0.8704	0.9817	0.9864	0.9654
IA	0.9688	0.9654	0.9955	0.9967	0.9914

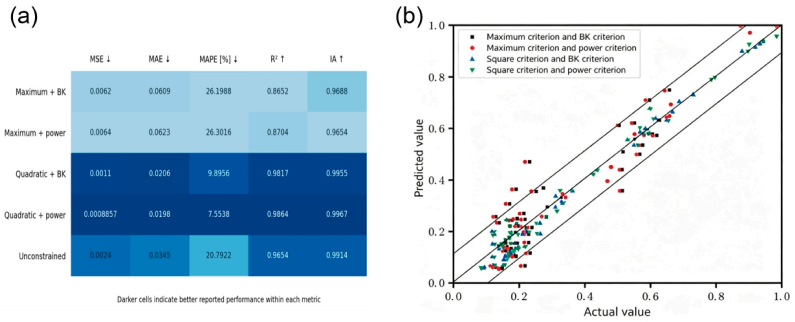


Figure 15. Comparison of the effects of different physical constraints on the predictive performance of neural network models: (**a**) comparison of the five performance metrics of the five prediction models; (**b**) comparison of predicted versus reference strength values with the ±10% error band.

4.3. Discussion

The quadratic initiation criterion includes the interaction between tensile peel and shear tractions, which is relevant to the mixed stress state near SLJ overlap ends. The power-law criterion then relates mixed-mode energy components to fracture resistance. Their combination is consistent with the cohesive formulation used to generate most samples, providing a plausible explanation for its lower reported errors. Maximum-stress and BK formulations remain valid alternatives. Their relative suitability depends on the material, calibration, and evaluation conditions.

A three-stage serial neural network model embedded with physical constraints was proposed in this study. In contrast to a monolithic network that attempts to learn the entire damage process in a single mapping, the serial architecture decomposes the problem into three physically meaningful subtasks. This decomposition reduces the complexity of each sub-mapping and mitigates overfitting when training data are scarce. It demonstrates superior performance compared to unconstrained models. This improvement is most pronounced in prediction stability. As shown in Figure 15, the predicted values cluster more tightly around the diagonal line. From a physical perspective, the serial architecture reflects the actual physical sequence of bonded structures. This sequence progresses from stress-induced damage initiation to ultimate failure induced by energy release. On the other hand, the criterion-based loss terms penalize inconsistency with the prescribed damage initiation and fracture conditions. This provides physical regularization of the intermediate predictions without guaranteeing exact physical admissibility.

A preliminary study was conducted by varying the number of hidden layers in each of the three interconnected MLPs from one to four. Among the configurations examined, single hidden layers with 100 neurons per layer provided the most favorable observed balance between prediction accuracy and computational efficiency [35,36]. Architectural selection also considered the ease of incorporating the physical constraints. Training hyperparameters were further refined through adjustments to the learning rate and gradient-update strategy. However, these investigations were limited in scope, and the width of 100 neurons was not established through a systematic neuron-count optimization. This configuration should therefore be regarded as a practical choice for the present dataset, with its applicability to other datasets requiring further validation.

5. Conclusions

In this study, the hygrothermal aging behavior and residual strength of composite bonded structures were investigated using experiments, finite element simulations, and machine learning methods. The following conclusions are drawn:

1. The adhesive layer's moisture absorption follows Fick's law. Both the equilibrium moisture uptake and the diffusion rate increase with temperature. The relationship between moisture absorption parameters and aging temperature is approximately linear.
2. The tensile strength and modulus of the adhesive decrease with increasing moisture uptake. For the SLJ structure, the shear strength exhibits a nonlinear decline during hygrothermal aging. The failure mode of the SLJ structure transitions from cohesive to interfacial as aging time and moisture absorption increase. The proportion of interfacial failures rose sharply from 19.74% to 87.27% during aging.
3. The established FE model, which couples moisture diffusion with a cohesive zone model (CZM), accurately simulates the evolution of the SLJ structure's mechanical properties. The simulation results show a calculation error of up to 5% relative to experimental data, verifying the model's accuracy.
4. A three-stage serial neural network model with physics-based loss constraints was proposed. The model incorporating physical constraints outperforms the original

model. The effects of different physical criteria on the prediction performance were compared. The results indicate that incorporating the quadratic stress and power-law criteria as loss constraints yields the best predictive performance. This approach significantly improves prediction stability and better aligns with the physical laws governing the evolution of adhesive layer damage.

Author Contributions: Conceptualization, W.F.; Methodology, X.-Q.R., J.-M.H. and W.F.; Validation, J.-M.H.; Formal analysis, X.-Q.R. and J.-M.H.; Investigation, J.-M.H. and W.F.; Data curation, J.-M.H.; Writing—original draft, X.-Q.R.; Writing—review & editing, Y.-Y.W., L.-L.L., G.-F.Z. and W.F.; Supervision, L.C., X.-H.N. and W.F.; Project administration, X.-Q.R. and W.F.; funding acquisition, X.-Q.R. and W.F. All authors have read and agreed to the published version of the manuscript.

Funding: This research was funded by the Independent Research Project Fund of the National Key Laboratory of Strength and Structure Integrity, grant number BYST-QZSYS-24-072; the National Natural Science Foundation for Young Scientists of China, grant number 12202336; and the Fundamental Research Funds for the Central Universities, grant number D5000230141.

Data Availability Statement: The data presented in this study were obtained from laboratory tests and are subject to confidentiality restrictions imposed by the project sponsor. The data are available from the corresponding author on reasonable request and with the approval of the sponsoring organization.

Conflicts of Interest: Author Jia-Mu He was employed by Xi'an ASN Technology Group Co., Ltd. The remaining authors declare that the research was conducted in the absence of any commercial or financial relationships that could be construed as a potential conflict of interest.

References

1. Zhao, Y.; Xuan, S.; Wang, Y.; Li, Y.; Yao, X. Reliability-based multi-objective optimization design of composite patch repair structure using artificial neural networks. *Compos. Struct.* **2025**, *352*, 118692. [CrossRef]
2. Chen, D.; Zhang, J.; Du, K.; Weng, M.; Bai, Z.; Li, C.; Shi, J. Hygrothermal aging effects on tensile strength of acrylic vs. epoxy adhesive CFRP lap joints: A comparative analysis. *Compos. Struct.* **2025**, *373*, 119699. [CrossRef]
3. Liu, Y.; Wang, H.; Ding, H.; Wang, H.; Bi, Y. Effect of hygrothermal aging on compression behavior of CFRP material with different layups. *Compos. Part B-Eng.* **2024**, *270*, 111134. [CrossRef]
4. Johar, M.; Chong, W.; Kang, H.; Wong, K. Effects of moisture absorption on the different modes of carbon/epoxy com-posites delamination. *Polym. Degrad. Stab.* **2019**, *165*, 117–125. [CrossRef]
5. Zhang, Y.; Ma, J.; Wu, C.; Han, X.; Zhang, W. Effects of moisture ingress on the mesoscale mechanical properties of epoxy adhesives under elevated temperature. *Polym. Test.* **2021**, *94*, 107049. [CrossRef]
6. Han, X.; Pickering, E.; Bo, A.; Gu, Y. Characterisation on the hygrothermal degradation in the mechanical property of structural adhesive: A novel meso-scale approach. *Compos. Part B Eng.* **2020**, *182*, 107609. [CrossRef]
7. Aicha, M.; Kouider, M.; Raul, D.S.; Campilho, G. Numerical analysis of the geometrical modifications effects on the tensile strength of bonded single-lap joints. *Int. J. Adhes. Adhes.* **2024**, *134*, 103814. [CrossRef]
8. Padmaraj, N.; Vijaya, K.M.; Dayananda, P. Experimental investigation on fatigue behaviour of glass/epoxy quasi-isotropic laminate composites under different ageing conditions. *Int. J. Fatigue* **2021**, *143*, 105992. [CrossRef]
9. Gusev, A.A.; Hine, P.J.; Ward, I.M. Fiber packing and elastic properties of a transversely random unidirectional glass/epoxy composite. *Compos. Sci. Technol.* **2000**, *60*, 535–541. [CrossRef]
10. Tang, Z.; Zhang, B. Prediction of biaxial failure envelopes for composite laminates based on Generalized Method of Cells. *Compos. Part B Eng.* **2012**, *43*, 914–925. [CrossRef]
11. Song, X.; Zhang, D.; Zhou, J.; Chen, X.; Zhang, S.; Bai, L.; Yang, X.; Du, F.; Guan, Z.; Zheng, X.; et al. Hierarchical multi-scale analysis of the effect of varying fiber bundle geometric properties on the mechanical properties of 3D braided composites. *Compos. Struct.* **2023**, *322*, 117375. [CrossRef]
12. Zhang, D.; Zhou, J.; Wang, J.; Zhang, W.; Guan, Z. A comparative study on failure mechanisms of open-hole and filled-hole composite laminates: Experiment and numerical simulation. *Thin-Walled Struct.* **2024**, *198*, 111730. [CrossRef]
13. Feng, W.; Xu, F.; Xie, W.; Zang, Y.; Zhang, X. Hygrothermal aging effects on the mechanical behavior of scarf-repaired composite laminates. *J. Adhes.* **2020**, *96*, 1233–1257. [CrossRef]
14. Zhang, Y.; Zhang, H. Multiscale finite element modeling of failure process of composite laminates. *Compos. Struct.* **2010**, *92*, 2159–2165. [CrossRef]

15. Song, J.-H.; Belytschko, T. Multiscale aggregating discontinuities method for micro-macro failure of composites. *Compos. Part B Eng.* **2009**, *40*, 417–426. [CrossRef]
16. Wang, J.; Zhang, C. Three-parameter, elastic foundation model for analysis of adhesively bonded joints. *Int. J. Adhes. Adhes.* **2009**, *29*, 495–502. [CrossRef]
17. Zheng, G.; He, Z.; Wang, K.; Liu, X.-L.; Luo, Q.; Li, Q.; Sun, G.-Y. On failure mechanisms in CFRP/Al adhesive joints after hygrothermal aging degradation following by mechanical tests. *Thin Wall Struct.* **2021**, *158*, 107184. [CrossRef]
18. Kailong, X.; Wei, C.; Xinying, Z.; Liu, L.; Zhao, Z.; Luo, G. Chemical, mechanical and morphological investigation on the hygrothermal aging mechanism of a toughened epoxy. *Polym. Test.* **2022**, *110*, 107548. [CrossRef]
19. Naghdabad, R.; Ghanbari, J. Hierarchical multiscale modeling of nanotube reinforced polymer composites. *Int. J. Multiscale Comput. Eng.* **2009**, *7*, 395–408. [CrossRef]
20. Xia, Z.; Zhang, Y.; Ellyin, F. A unified periodical boundary conditions for representative volume elements of composites and applications. *Int. J. Solids Struct.* **2003**, *40*, 1907–1921. [CrossRef]
21. Icardi, U.; Sola, F. Analysis of bonded joints with laminated adherends by a variable kinematics layerwise model. *Int. J. Adhes. Adhes.* **2014**, *50*, 244–254. [CrossRef]
22. Kibrete, F.; Trzepieciński, T.; Gebremedhen, H.S.; Woldemichael, D.E. Artificial intelligence in predicting mechanical properties of composite materials. *J. Compos. Sci.* **2023**, *7*, 364. [CrossRef]
23. Yan, H.; Deng, Z. Prediction of properties of short fiber reinforced urethane polymer composites based on deep learning. *Acta Mater. Compos. Sin.* **2019**, *36*, 1413–1420.
24. Mu, W.; Chen, X.; Li, S.; Na, J. Machine learning-based assessment of hygrothermal aging performance in CFRP-aluminum alloy adhesive bonded structures. *J. Adhes.* **2024**, *100*, 1040–1065. [CrossRef]
25. Hu, H.; Qi, L.; Chao, X. Physics-informed Neural Networks (PINN) for computational solid mechanics: Numerical frameworks and applications. *Thin-Walled Struct.* **2024**, *205*, 112495. [CrossRef]
26. *ISO 527-2:2012*; Plastics-Determination of tensile properties-Part 2: Test conditions for moulding and extrusion plastics. International Organization for Standardization (ISO): Geneva, Switzerland, 2012.
27. Feng, W.; Chang, L.; He, J.; Daiz, Z.; Shi, X.; Xie, W.; Xu, F. A nanomodified-ultrasonic method to improve the shear strength of adhesively bonded com-posite joints. *Compos. Part A Appl. Sci. Manuf.* **2024**, *187*, 108483. [CrossRef]
28. Saidane, E.H.; Scida, D.; Assarar, M.; Ayad, R. Assessment of 3D moisture diffusion parameters on flax/epoxy composites. *Compos. Part A Appl. Sci. Manuf.* **2016**, *80*, 53–60. [CrossRef]
29. Heshmati, M.; Haghani, R.; Al-Emrani, M. Effects of moisture on the long-term performance of adhesively bonded FRP/steel joints used in bridges. *Compos. Part B-Eng.* **2016**, *92*, 447–462. [CrossRef]
30. Turon, A.; Camanho, P.P.; Costa, J.; Dávila, C.G. A damage model for the simulation of delamination in advanced composites under variable-mode loading. *Mech. Mater.* **2006**, *38*, 1072–1089. [CrossRef]
31. Feng, W.; Cheng, Y.; Zhang, Q.; Liu, G.; Li, L.; Cheng, Z.; Xu, F. Quantitatively determining the local effect of hygrothermal aging on the creep behaviour of epoxy adhesives. *Polym. Test.* **2026**, *159*, 109197. [CrossRef]
32. Álvarez, D.; Blackman, B.R.K.; Guild, F.J.; Kinloch, A.J. Mode I fracture in adhesively-bonded joints: A mesh-size independent modelling approach using cohesive elements. *Eng. Fract. Mech.* **2014**, *115*, 73–95. [CrossRef]
33. Rahman, M.M. Characterization and predictive modeling of thermally aged glass fiber reinforced plastic composites. *Res. Eng. Struct. Mater.* **2024**, *10*, 305–330. [CrossRef]
34. Wang, B.; Huang, K.; Guo, L. A two-stage deep learning framework for predicting crack patterns and mechanical properties of unidirectional composites with void defects. *Compos. Sci. Technol.* **2025**, *271*, 111357. [CrossRef]
35. Srinath, E.; Venkateswara Reddy, K.; Manohar, G.; Kumar, P.P.; Ashok, N. Data-driven prediction of microhardness and tensile strength in microwave-sintered ZrC reinforced AA7075/SiC hybrid composites using machine learning. *Sci. Rep.* **2026**, *16*, 15971. [CrossRef] [PubMed]
36. Brito Oliveira, G.A.; Freire Júnior, R.C.S.; Barbosa, J.F.; Correia, J.A. An approach to predict ultimate transverse tensile strength based on mixed ANN models for a composite lamina. *J. Mater. Res. Technol.* **2023**, *23*, 2719–2729. [CrossRef]

Disclaimer/Publisher's Note: The statements, opinions and data contained in all publications are solely those of the individual author(s) and contributor(s) and not of MDPI and/or the editor(s). MDPI and/or the editor(s) disclaim responsibility for any injury to people or property resulting from any ideas, methods, instructions or products referred to in the content.